



Enhanced ethyl acetate sensing performance of Al-doped In_2O_3 microcubes



Jingli Shen^a, Feng Li^a, Bo Yin^a, Liang Sun^c, Chuan Chen^c, Shanpeng Wen^a, Yu Chen^{a,c,**}, Shengping Ruan^{b,*}

^a State Key Laboratory on Integrated Optoelectronics and College of Electronic Science & Engineering, Jilin University, Changchun 130012, PR China

^b State Key Laboratory on Applied Optics, Changchun 130023, PR China

^c Global Energy Interconnection Research Institute, Beijing, 102211, PR China

ARTICLE INFO

Article history:

Received 20 December 2016

Received in revised form 16 April 2017

Accepted 22 June 2017

Available online 23 June 2017

Keywords:

Al doping

Ethyl acetate

Gas sensor

ABSTRACT

In_2O_3 and 2.5–10 at% Al-doped In_2O_3 are prepared through a simple solvothermal method, and samples are characterized by a variety of methods to investigate the phase and morphological properties. The gas sensing measurements reveal that Al-doped In_2O_3 has superior ethyl acetate sensing capability as compared to pure In_2O_3 , with the maximum response value approaching 56.3–100 ppm ethyl acetate at 184 °C, which is about 2.34 times higher than pure In_2O_3 . In addition, 5 at% Al-doped In_2O_3 gas sensor is also found to have lower detection limit and better selectivity to ethyl acetate. Hence, Al-doped In_2O_3 material can be promising for sensing ethyl acetate gas with high performance. Also, the mechanism involved in improving sensing performance of Al-doped In_2O_3 is discussed.

© 2017 Elsevier B.V. All rights reserved.

1. Introduction

Cancer has become a leading cause of death worldwide, especially in North America, Europe and Australia. Early detection has been proven to be a highly effective approach to increase the curative ratio. Many medical equipments have been explored, and one of them is through the breath test. Comparing with other counterparts, the breath test can be operated easily and with minimal invasion [1,2]. The use of breath test in illness detection is a rapidly developing area, because every kind of disease patients exhale special gases, such as acetone (in the case of diabetics), nitric oxide (in the case of asthma) and ammonia (in the case of renal diseases) [3]. Among various gas sensors, the ethyl acetate gas sensor has become vital since both colorectal and gastric cancer patients exhale this kind of gas and these two kinds of cancer are listed on the top five cancers due to the notorious high death rate [4]. Moreover, ethyl acetate gas sensor can be used in meat aging process. The quality control of meat is totally different from the case of fish which is as fresh as possible after being caught. However,

meat needs to undergo an aging process for optimal eating quality. And ethyl acetate is a major product at the initial stage of bacterial putrefaction [5]. Ethyl acetate is broadly used as industrial solvents and extractant of volatile organic compounds (VOCs). Inhalation of 400 ppm ethyl acetate can cause acute toxicity and ethyl acetate concentration over 2% in the atmosphere can cause blast. With the development of industry, the demand for ethyl acetate is growing fast, which will increase the risk to workers. Therefore, the development of low-cost, ultrasensitive, highly selective and convenient gas sensors, which can sense microscale amounts of ethyl acetate, has become vital to biomedical applications, food industry and environmental monitoring.

In light of the attractive advantages of easy fabrication, low power consumption and high sensitivity, gas sensors based on semiconductor oxides have shown potential and been regarded as commendable approach in the monitoring atmosphere [6]. In recent years, several semiconductor oxides such as SnO_2 , In_2O_3 , Fe_2O_3 , ZnO and TiO_2 have been extensively investigated as gas sensor materials [7–14]. Among these, In_2O_3 is one of the widely studied sensing materials for detection of NO_2 [15], $\text{CH}_3\text{CH}_2\text{OH}$ [16], CO [17], O_3 [18] and has been widely applied in window heaters, liquid-crystal displays and solar cells [19–21]. The basic sensing principle of semiconductor oxide-based gas sensors is that their resistance will change when exposed to different gas atmosphere. Hence semiconductor oxides' chemical composition,

* Corresponding author.

** Corresponding author at: State Key Laboratory on Integrated Optoelectronics and College of Electronic Science & Engineering, Jilin University, Changchun 130012, PR China.

E-mail addresses: Chenyu@semi.ac.cn (Y. Chen), ruansp@jlu.edu.cn, zhoujr@jlu.edu.cn (S. Ruan).

crystalline size and microstructure have significant impact on sensing performances [22].

Ethanol is one of the most representative gases that can be detected in a selective manner using semiconductor oxide probably because of its high reactivity. In contrast, there are few journals about ethyl acetate gas sensor. Naomi et al. reported that Rh-La₂O₃-In₂O₃ gas sensor displayed a sensitivity of 100 for 300 ppm ethyl acetate at 300 °C [5]. Xiaoan et al. studied the sensor based on Y₂O₃-nanoparticles for 3600 ppm at 264 °C [23].

In this report, In₂O₃ and Al-doped In₂O₃ were synthesized by a facile hydrothermal route. The prepared In₂O₃ showed high response to ethyl acetate. To enhance gas sensing properties, Al was introduced into In₂O₃. As expected, it was revealed that Al-doped In₂O₃ showed much higher response, lower detection limit and better selectivity to ethyl acetate than pure In₂O₃. The dramatic improvement in gas sensing properties might be caused by larger chemical potential gradient, more electrons transfer and the changes in grain size. The results confirmed that Al-doped In₂O₃ gas sensor was a promising candidate for detecting ethyl acetate.

2. Experimental

2.1. Chemical reagents

Indium nitrate tribasic hydrate was obtained from Sinopharm Chemical Reagent CO. Ltd. Aluminum chloride and sodium hydroxide were purchased from Beijing Chemical Works. Polyvinylpyrrolidone was purchased from Aladdin Chemistry CO.Ltd. All chemical reagents involved in the experiment were analytical grade and directly used without any further purification.

2.2. Preparation of pure and Al-doped In₂O₃

The pure and Al-doped In₂O₃ with doping concentration of 2.5, 5 and 10 at% were synthesized by hydrothermal procedure, labeled as S0, S1, S2 and S3. Generally, 1.18 g Indium nitrate tribasic hydrate ($\text{In}(\text{NO}_3)_3 \cdot 4.5\text{H}_2\text{O}$) was dissolved into a mixture solution of 50 mL deionized water and 10 mL ethanol under vigorously stirring. Then 0.08 g PVP(MW = 1300000), 0.01 g sodium hydroxide (NaOH) and different amounts of aluminum chloride (AlCl₃) were added into the before-mentioned solution under constant stirring. After 6 h vigorous stirring, the transparent solutions were transferred into Teflon-lined stainless steel autoclaves, which were heated at 180 °C for 18 h and then cooled to room temperature. The products were collected by centrifugation, washed by deionized water and ethanol five times and dried at 60 °C for 12 h. Finally the products were annealed at 600 °C for 2 h.

2.3. Characterization

The materials were characterized by X-ray power diffraction (XRD), X-ray photoelectron spectroscopy (XPS), energy dispersive X-ray spectrogram (EDX), scanning electron microscopy (SEM) and transmission electron microscope (TEM). The specific surface area was estimated using the Brunauer-Emmett-Teller (BET) equation based on the nitrogen adsorption isotherm obtained with Micromeritics Gemini VII apparatus. XRD was performed on a Scintag XDS-2000 X-ray diffractometer with Cu K α radiation ($\lambda=1.5418 \text{ \AA}$). XPS data was obtained from Scienta ESCA200 spectrometer equipped with Al K α radiation source. SEM images and EDX were gained using a SHIMADZU SSX-550 (Japan) instrument. TEM images were obtained on a JEM-ARM200F.

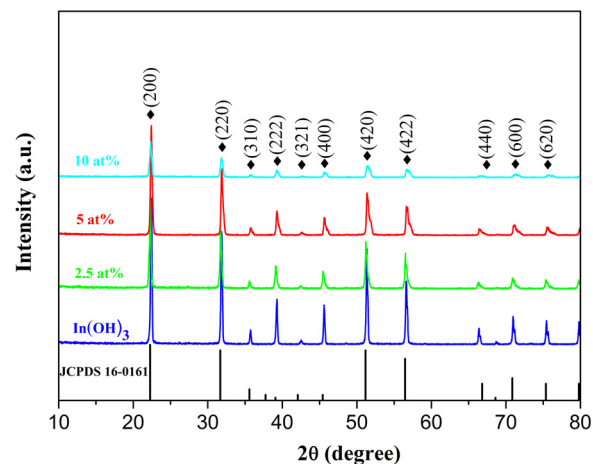


Fig. 1. XRD patterns of pure and Al-doped In(OH)₃.

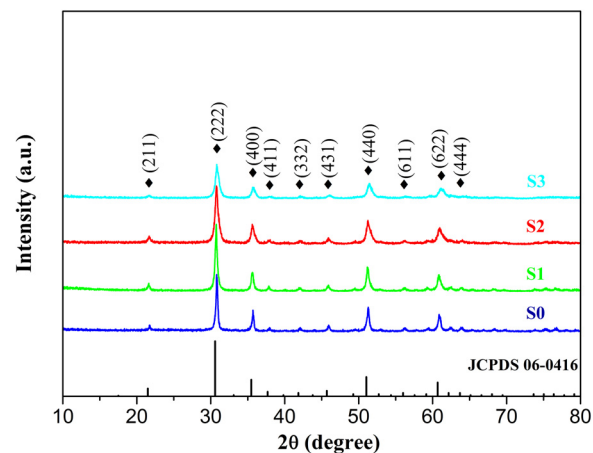


Fig. 2. XRD patterns of pure and Al-doped In₂O₃.

2.4. Fabrication and measurement of sensors

The prepared material was mixed with deionized water at a weight ratio of 5:1 and grinded in a mortar for a while. Then the paste was coated on the surface of alumina ceramic tube with gold electrodes fabricated by jetting Au paste through a metal-jetting system (MJ-10, Beijing Elite Tech Co., Ltd., China). After that a Ni-Cr heating coil was inserted through the ceramic tube to form a side-heated gas sensor.

Gas sensing behavior was estimated by CGS-8 intelligent gas sensing analysis system (Beijing Elite Tech Co. Ltd., China). The specific measurement was processed by a static process: the sensor was placed in a glass chamber full of fresh air at the beginning and then appropriate amount of test gas was injected into the closed chamber by a micro-injector. After the response reaching a steady value, the sensor was transferred into another chamber also full of air and began to recover. The gas-sensing properties were tested under the same condition (RH: 30%; room temperature). The gas response S ($S = R_a/R_g$) was defined as the ratio of sensor resistance in air (R_a) to that in the test gases (R_g).

3. Results and discussion

3.1. Characterization

To investigate the phase identification and crystal sizes, the XRD patterns were shown in Figs. 1 and 2. Fig. 1 showed the XRD patterns

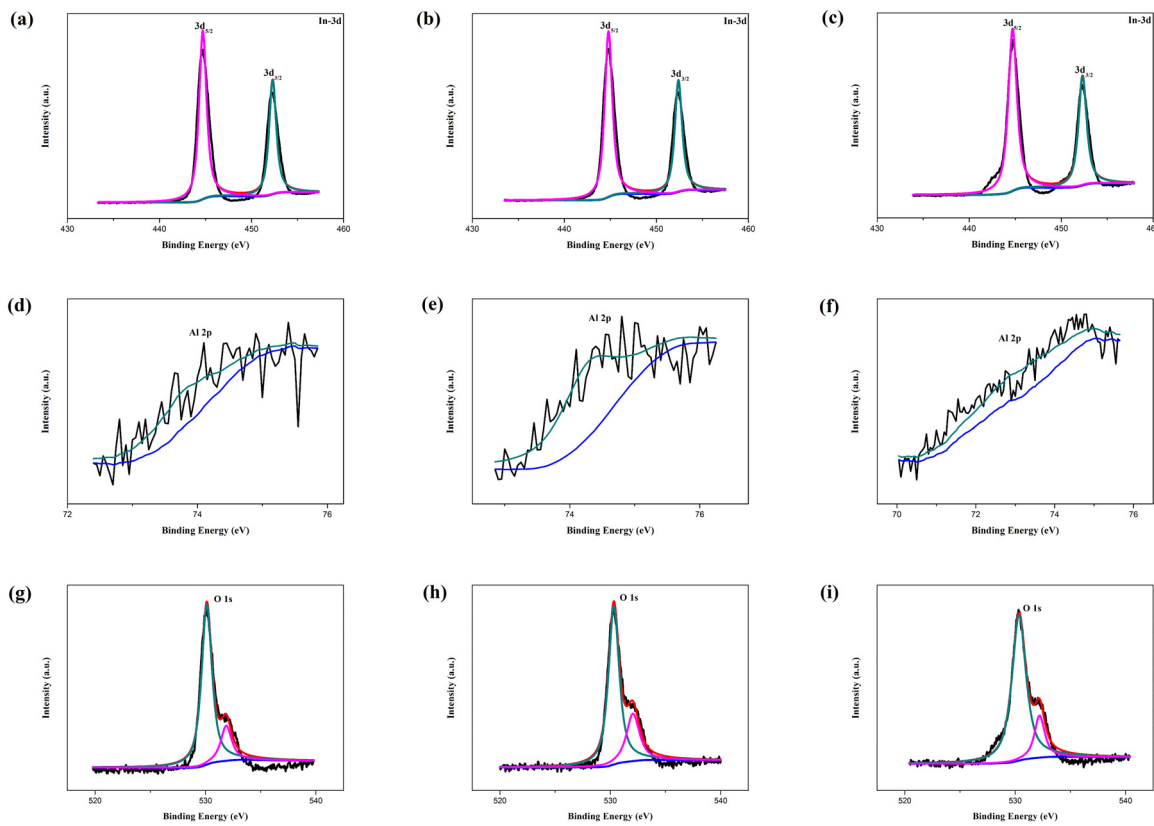


Fig. 3. XPS spectra for S1: (a,d,g), S2: (b,e,h) and S3: (c,f,i).

of as-synthesized powder at different atomic rate of In:Al. All peaks could be well-assigned to the (200), (220), (222), (420), (422) planes of In(OH)_3 , which confirmed to No.16-0161 of the Joint Committee on Powder Diffraction Standards card (JCPDS) and no other phases corresponding to aluminum or aluminum compound were found in the XRD patterns after adding aluminum material. Fig. 2 showed XRD patterns of as-prepared powder at different atomic rate of In:Al. All peaks were well-assigned to the single phase of In_2O_3 (JCPDS, 06-416) for both undoped and Al-doped In_2O_3 materials. Besides, the crystallinity of the Al-doped In_2O_3 samples decreased and the diffraction peaks became broader with more aluminum ions. It indicated that Al ions incorporated into the lattice of In_2O_3 without significantly destroying the cubic structure of indium oxide rather than generating crystalline phases of aluminum oxides. Doping did not change the crystal structure but it caused the change of the lattice constant. It could be observed that (222), (400), (431), (440), (622) peaks position shifted to the right with more Al doping. It was caused by the radius of Al ions (0.0535 nm) was smaller than that of In ions (0.08 nm).

The average grain size of S0, S1, S2 and S3 was calculated by using Scherer's equation,

$$D = \frac{0.89 \times \lambda}{\beta \times \cos\theta} \quad (1)$$

where λ is X-ray wavelength, θ is Bragg diffraction angle and β is the peak width at half maximum. The average crystal size of pure, 2.5 at%, 5 at% and 10 at% Al-doped In_2O_3 was about 34.6 nm, 32.1 nm 20.7 nm and 17.2 nm, respectively. It could be found that the crystal sizes were decreasing continually with increasing the amount of Al.

We evaluated the lattice constants of pure and Al-doped In_2O_3 according to Bragge's law:

$$n\lambda = 2ds\sin\theta \quad (2)$$

where, n is the order of diffraction (usually $n=1$), λ is X-ray wavelength and d is the spacing between planes of given Miller indices h, k, l . In the cubic structure of In_2O_3 , the plane spacing is related to lattice constant and Miller indices by the following formula:

$$\frac{1}{d_{(hkl)}^2} = \frac{h^2 + k^2 + l^2}{a^2} \quad (3)$$

According to the above formula, for the (100) orientation, the lattice constant a is calculated by

$$a = \frac{\sqrt{3}\lambda}{\sin\theta} \quad (4)$$

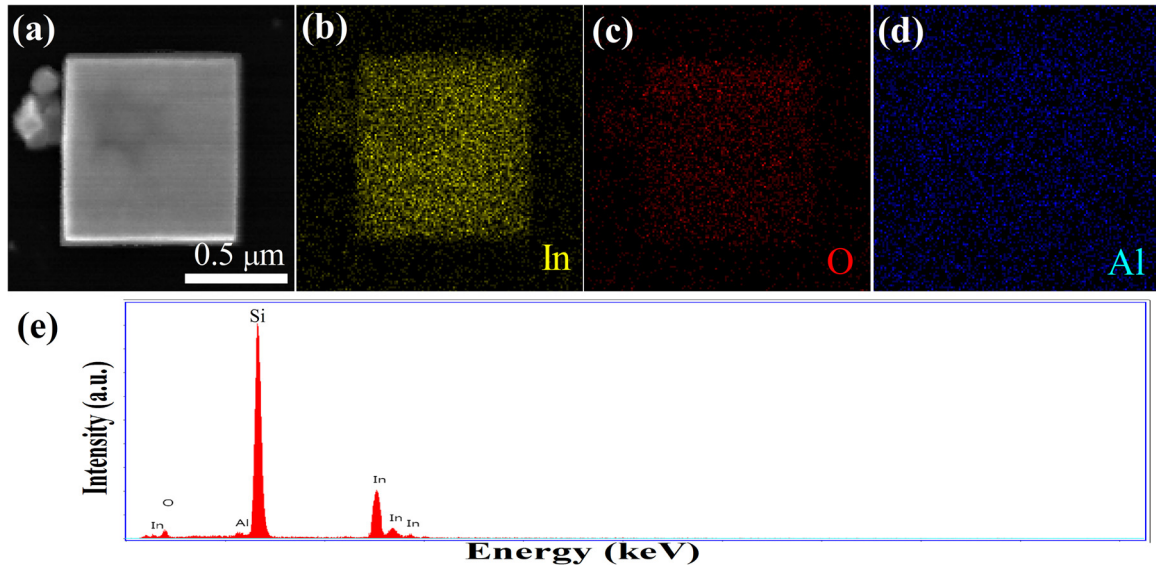
It could be calculated that the lattice constant a was 1.00733 nm, 1.00697 nm, 1.00504 nm, 1.00454 nm for pure, 2.5 at%, 5 at% and 10 at% Al-doped In_2O_3 , respectively. When In^{3+} ions were replaced by Al^{3+} ions, a decrease in the lattice constants a was expected, which would lead to a decrease in grain size.

Fig. 3 showed high-resolution XPS spectra of In 3d, O 1s and Al 2p for S1, S2 and S3. The binding energies of $\text{In 3d}_{5/2}$ and $\text{In 3d}_{3/2}$ were listed in Table 1. Compared with pure In_2O_3 (444.6 eV for $\text{In 3d}_{5/2}$ and 452.1 eV for $\text{In 3d}_{3/2}$), the binding energies of S1, S2 and S3 had an obvious increase. The chemical shifts of binding energies reflected the electronic interaction between the In_2O_3 and dopant [24]. The spin orbit splitting of In 3d was 7.54, which indicated the indium was in the form of oxide [25,26]. Fig. 3(d-f) showed the high resolution scan of Al 2p for S1, S2 and S3. The peaks were located in 74.15 eV, 74.35 eV and 74.52 eV, respectively. Compared with the peak at 74.6 eV of pure Al_2O_3 , all of the peaks shifted to the low binding energies which indicated that Al was doped into In_2O_3 [27,28]. The In/Al mole ratio of S1, S2 and S3 was about 19.7:1, 12.9:1 and 6.9:1, respectively. As S1, S2 and S3 are surface resistance-type sensing materials, the capacity of adsorbing oxygen onto the surface of the semiconductor oxides materials has

Table 1

XPS analysis results of S1, S2 and S3.

Sample	In3d _{5/2}	In3d _{3/2}	Al2p	O _L	O _C	Peak (eV)	Relative Percentage (%)
	Peak (eV)	Peak (eV)	Peak (eV)	Peak (eV)			
S1	444.71	452.25	74.15	530.12	82.32	531.87	18.68
S2	444.79	452.34	74.35	530.31	73.47	532.05	26.53
S3	444.81	452.35	74.52	530.34	81.05	532.17	18.95

**Fig. 4.** SEM and EDX images of 5 at% Al-doped In_2O_3 .

a great influence on the gas sensing ability by changing the thickness of the depletion layer. Therefore the O 1 s XPS spectrums were measured and exhibited in Fig. 3. In order to verify the status of oxygen species, the tested curves of S1, S2 and S3 could be decomposed into two fitted peaks, which indicated that the samples had two kinds of significant oxygen species [29]. Lattice oxygen species and chemisorbed oxygen species were expressed with O_L and O_C, respectively. Table 1 listed the center positions of all elements and the relative percentages of each oxygen species. It could be found that the relative percentage of the O_C component of S2 had an obvious promotion comparing with that of S1 and S3, which meant the surface oxygen chemisorbed ability of S2 was higher than that of S1 and S3. The increase of O_C component meant that more surface chemisorbed oxygen species could participate in the redox reaction occurring on the surface of the sensing materials and thus cause a larger change in sensor resistance. According to XRD and XPS spectrum, it was reasonable to conclude that In^{3+} ions in the In_2O_3 lattice were substituted by Al^{3+} ions.

Fig. 4 showed the elemental map and spectra of the S2. Fig. 4(a) was SEM image of S2. Fig. 4(b-d) showed the element distribution and proved the existence of the In, O and Al elements. From the elemental map, it could be known that the distribution of the In, O and Al elements was uniform. The spectra shown in Fig. 4(e) confirmed the existence of the elements Si, O, Al and In. As-prepared powder was pasted on the silicon wafer. It caused the Si element signal was observed in the spectrum.

To get a deeper understanding of the size and morphology, SEM and TEM images were introduced. Fig. 5(a-d) showed the low-magnification images of as-synthesized powder at different atomic rate of In:Al. From the SEM images, it could be observed that as-synthesized microcubes surface was smooth and size become larger with the increasing of Al ratio. Fig. 6(a-d) showed SEM images of the pure, 2.5 at%, 5 at%, 10 at% Al-doped In_2O_3 . The typical SEM images

of resulting products revealed that calcination did not change morphology and size. Smooth surface turned into crannied and coarse surface after calcination. At high calcination temperature, $\text{In}(\text{OH})_3$ turned to In_2O_3 by evaporation of water molecules. As the thermal stability of $\text{In}(\text{OH})_3$ was lower than In_2O_3 , the In-OH bond broke down at high calcination temperature. Fig. 7 showed SEM and TEM images of S2. As shown in Fig. 7(a,b), the microcube was crannied and hollow. Therefore, gas molecules could pass through the materials and react in the materials. HRTEM result was displayed in Fig. 7(c). The lattice fringes could be clearly observed and the lattice spacing was 0.292 nm, corresponding to the (222) planes of In_2O_3 .

The specific surface area of pure and Al-doped In_2O_3 was evaluated by nitrogen adsorption-desorption measurements. The representative nitrogen adsorption-desorption isotherm and the corresponding BJH pore size distribution plot were given in Fig. 8 and the inset. The adsorption-desorption isotherm exhibited an obvious hysteresis loop and could be indexed as type-IV isotherm according to the International Union of Pure and Applied Chemistry (IUPAC) classification. The BET surface area of pure and 5 at% Al-doped In_2O_3 were calculated to be $9.39 \text{ m}^2 \text{ g}^{-1}$ and $19.91 \text{ m}^2 \text{ g}^{-1}$ respectively, and the BJH pore size distribution was mainly concentrated in the 2–20 nm range. The material reacted with its surrounding mainly via its surface. Therefore, the higher specific surface area of S2 could adsorb more molecules and lead to the improved performances.

3.2. Growth mechanism

A reasonable growth mechanism of In_2O_3 microcubes could be illustrated by Fig. 9. In the reaction process, $\text{In}(\text{NO}_3)_3 \cdot 4.5\text{H}_2\text{O}$ and NaOH served as the sources of In^{3+} and OH^- ions, respectively. When PVP was added into the system, the reaction pairs of In^{3+} and O^{2-} in PVP units occupied the empty mental orbits in the solution,

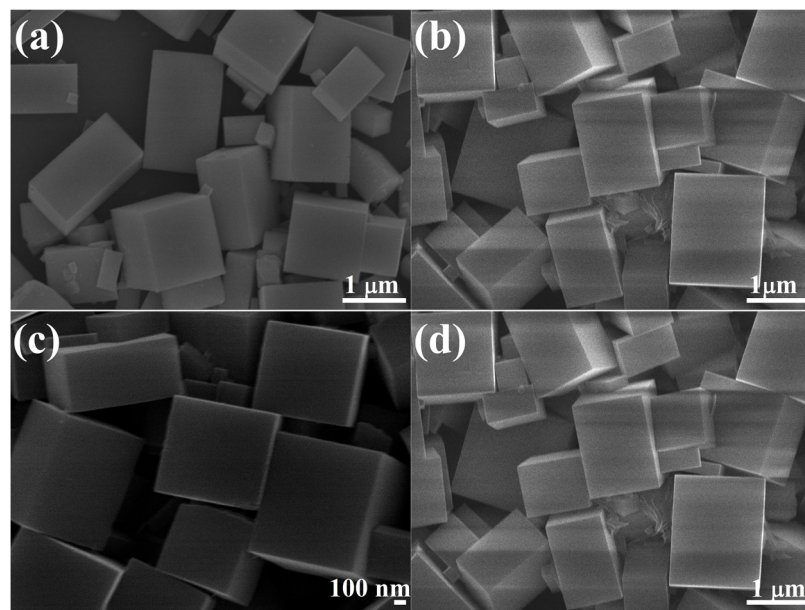


Fig. 5. SEM images of (a) pure $\text{In}(\text{OH})_3$, (b) 2.5 at% Al-doped $\text{In}(\text{OH})_3$, (c) 5 at% Al-doped $\text{In}(\text{OH})_3$, (d) 10 at% Al-doped $\text{In}(\text{OH})_3$.

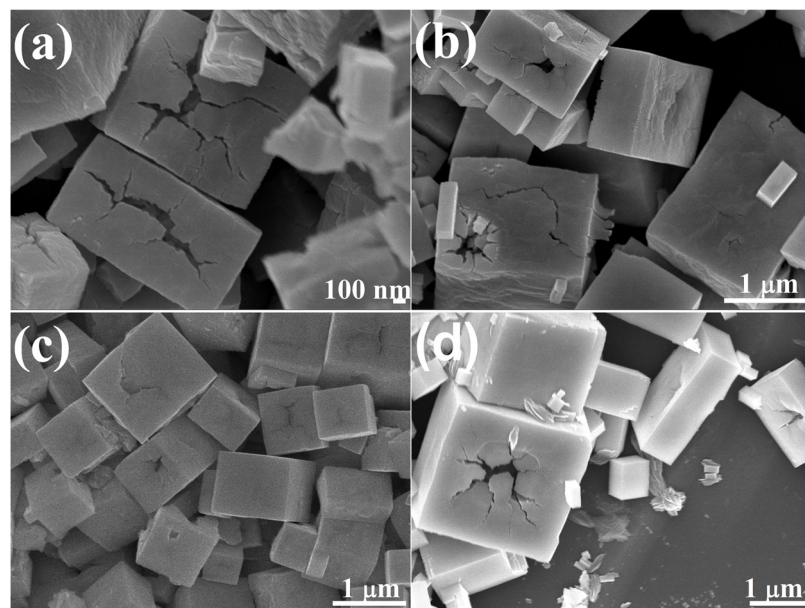


Fig. 6. SEM images of (a) pure In_2O_3 , (b) 2.5 at% Al-doped In_2O_3 , (c) 5 at% Al-doped In_2O_3 , (d) 10 at% Al-doped In_2O_3 .

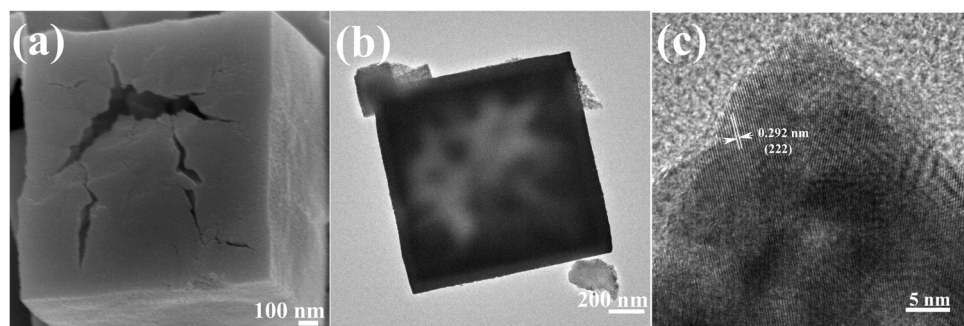


Fig. 7. (a) SEM image of S2, (b) TEM image of S2, (b) HRTEM image taken from (b).

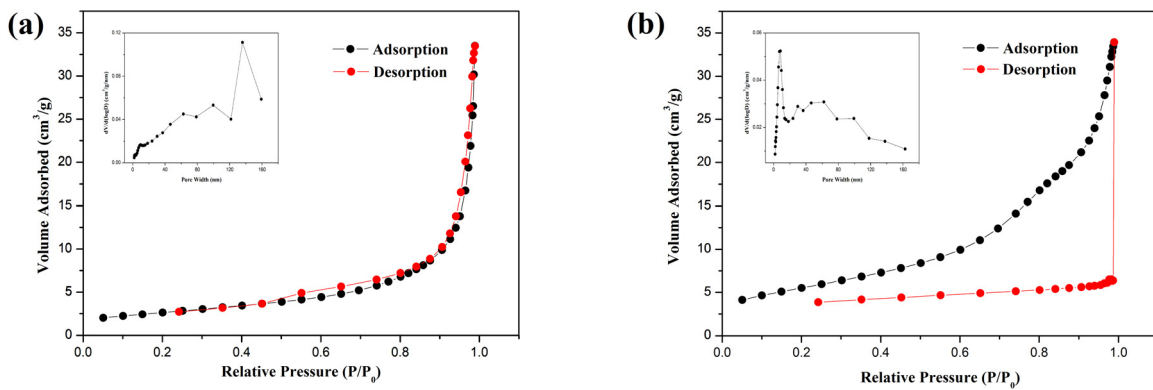


Fig. 8. Nitrogen adsorption-desorption isotherm and corresponding BJH pore size distribution (inset): (a) S0, (b) S2.

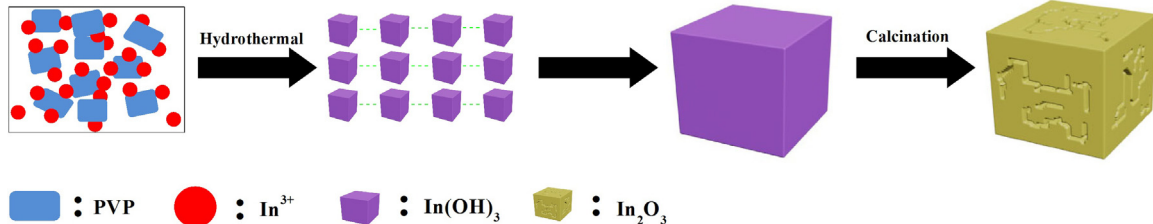


Fig. 9. The schematic of the growth mechanism of In_2O_3 microcubes.

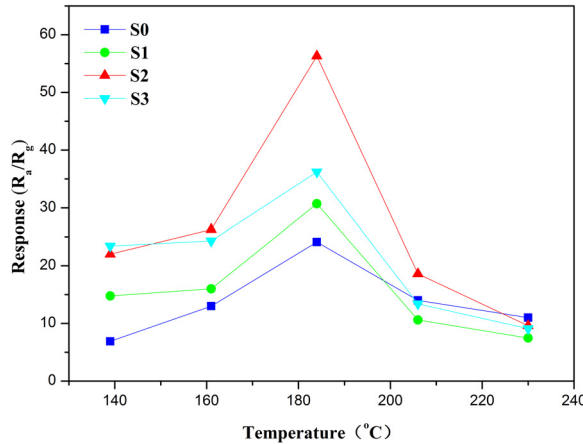


Fig. 10. Response of sensors based on S0, S1, S2 and S3 to 100 ppm ethyl acetate as function of operating temperature.

to form coordinate bonds between In^{3+} and PVP [30,31]. Under the hydrothermal conditions, In^{3+} would gradually be converted into $\text{In}(\text{OH})_3$ crystal nucleus [32]. To decrease the free energy, the crystal nuclei of $\text{In}(\text{OH})_3$ gradually grew into large cubes through Ostwald ripening process [33,34]. Then In_2O_3 microcubes was obtained by calcination of $\text{In}(\text{OH})_3$ precursor. When Al^{3+} ions were added into the solution, some of In^{3+} ions in $\text{In}(\text{OH})_3$ were substituted by Al^{3+} ions and finally Al-doped In_2O_3 microcubes was obtained.

3.3. Gas sensing properties

In the gas-sensing research, the operating temperature played an important role in determining the gas-sensing properties due to its impact on surface state of sensing materials and interaction between the absorbed oxygen and sensing materials [35]. So we investigated the relationships between the operating temperatures and gas responses to 100 ppm ethyl acetate of pure and Al-doped In_2O_3 , which was shown in Fig. 10. At low temperature

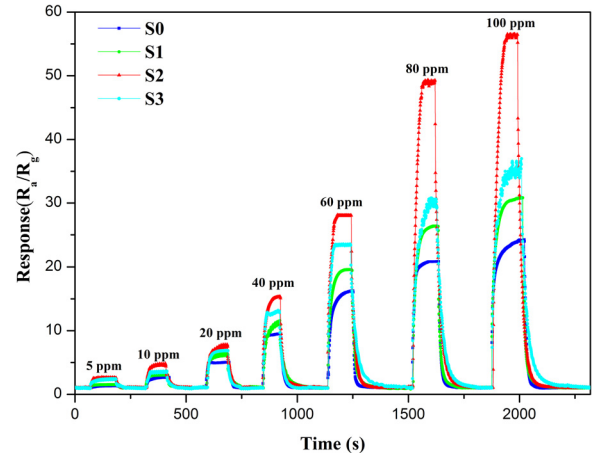


Fig. 11. The dynamic response of S0, S1, S2 and S3 to 5–100 ppm ethyl acetate.

ethyl acetate molecules did not have enough energy to overcome activation energy barrier to react with the surface adsorbed oxygen species. If the temperature was too high, the surface had difficulty in gas adsorption [36–38]. So it could be observed that the response of the tested sensor increased first until the response topped and then decreased with the temperature increasing. For pure In_2O_3 , the maximum response was 24.1, while in the 5 at% Al-doped In_2O_3 composite case, the maximum response was 56.3, which was about 2.34 times higher than pure In_2O_3 . Accordingly, 184 °C was selected as optimum operating temperature for the four gas sensors and applied in all investigations thereafter.

Fig. 11 displayed the response of sensors based on pure and Al-doped In_2O_3 to ethyl acetate with various concentrations from 5 to 100 ppm at operating temperature. All sensors exhibited an increase of response with increasing ethyl acetate concentration and it was worth noting that gas sensors were all improved after Al-doping. When S2 was exposed to 5 ppm ethyl acetate, the response value was 2.64 indicating the detectable ethyl acetate minimum

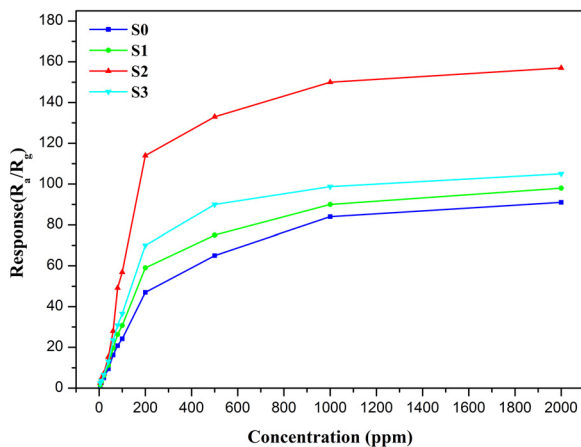


Fig. 12. Response of sensors based on S0, S1, S2 and S3 versus ethyl acetate concentrations (5–2000 ppm).

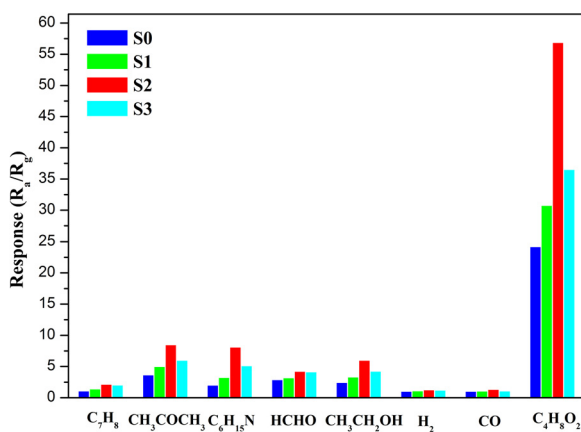


Fig. 13. Response of S0, S1, S2 and S3 exposed to 100 ppm different gases at 184 °C.

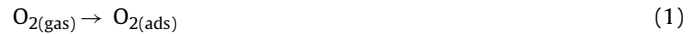
limit was 5 ppm. For S0, S1 and S3 sensors, their detectable minimum limit was 10 ppm. Fig. 12 presented the relation curves between responses and concentration of ethyl acetate at operating temperature. Ethyl acetate concentration ranged from 5 to 2000 ppm. The response increased rapidly with increasing of ethyl acetate concentration and then gradually tended to saturation when gas concentration reached 1000 ppm. From the curves, it could be clearly seen that S2 exhibited the highest response to 5–2000 ppm ethyl acetate compared with S0, S1 and S3.

Since selectivity was an important aspect of sensing properties, pure, 2.5, 5 and 10 at% Al-doped In_2O_3 to 100 ppm of various test gases were investigated at operating temperature and the results were shown in Fig. 13. Evidently, four gas sensor devices exhibited much higher response to ethyl acetate than other test gases, proving the good selectivity for ethyl acetate. In addition, it was worth indicating that S2 exhibited highest response to all gases and the largest increase could be observed for ethyl acetate. So it was concluded that 5 at% Al-doping caused a remarkable enhancement and excellent selectivity in sensing properties.

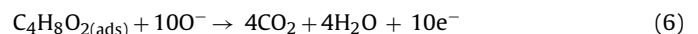
3.4. Gas sensing mechanism

As typical *n*-type semiconductor oxides, the most accepted sensing mechanism is surface controlled model. It is based on resistance change which is caused by the adsorption and desorption process under different gas surroundings [39–41]. When In_2O_3 was exposed to air, it could adsorb oxygen molecules on the surface and O_2 would trap free electrons from the conduction band to form

negative oxygen ions (O_2^- , O^- and O^{2-}) [42]. Then a thick electron depletion layer was formed on the surface area, resulting in a decrease of carrier concentration and increase of sensor resistance. The following equations could describe the reactions [43].



When In_2O_3 based sensor was exposed to test gas, the adsorbed oxygen species (O_2^- , O^- and O^{2-}) would react with test gas molecules to form CO_2 and H_2O . Then electrons, which trapped in the ionized oxygen species, would be released back to the conduction band. It caused increase of charge carriers and decrease of resistance. It could be explained by following reactions



It was clearly revealed that Al-doped In_2O_3 sensors exhibited much better sensing performances than pure In_2O_3 , indicating Al doping contributed greatly to the improvement of sensing properties. The reason for the enhancement in gas sensing performance of Al-doped In_2O_3 gas sensor may be as follows. First, it can be explained in terms of the transfer of electrons from ethyl acetate gas molecule to the microcubes due to the chemical potential gradient between In_2O_3 and ethyl acetate. The existence of the native defects such as metal interstitials and oxygen vacancies causes as-grown In_2O_3 behaves as *n*-type semiconductor. Fig. 14 shows the energy band diagram of pure In_2O_3 and Al-doped In_2O_3 , where E_C , E_V and E_F correspond to the conduction band, the valence band and the Fermi level of In_2O_3 . In the energy band diagram, the position of E_F is nearer to E_C for pure In_2O_3 . After Al doping, E_F could be slightly shifted to E_V (Fig. 14(b)) (the Al-doped sensor maintained a higher resistance than pure In_2O_3) compared to pure In_2O_3 energy band diagram (Fig. 14(a)). The chemical potential level μ_{EA} is drawn for ethyl acetate to represent the chemical potential of the electrons present in the gas molecule that can participate in the electron transfer process. The electron depletion region, which is caused by adsorbed oxygen capturing electrons, exists near the surface of microcubes. When ethyl acetate is adsorbed onto the microcubes surface, electrons will start transferring from the higher chemical potential to the material with the lower chemical potential. It will stop, when the system reaches equilibrium. The pure In_2O_3 possesses a smaller chemical potential gradient (the absorbed ethyl acetate and the pure In_2O_3) compared to Al-doped In_2O_3 . It causes less electrons transfer and then lower sensitivity. The second is that crannied and coarse surface provides a high surface area and increases the amount of test gas absorbed onto the surface. Synchronously, the gas diffusion toward the entire sensing surface is not hampered. Thirdly, from the XRD patterns, it could be observed that Al doping effectively controls the In_2O_3 grain growth. It causes more sensitive sites on the grain boundaries exposing to test gas, which is beneficial for sensitivity of gas sensing. Hence, Al-doped In_2O_3 exhibited much better sensing performances than pure In_2O_3 .

The gas-sensing properties of materials are closely related to their structures. Al-doping can increase the active center sites of surface, which makes the ethyl acetate adsorption easier [44–46]. So the increase of Al dopant leads to the enhancement in selectivity. Further augment of Al dopant does not result in better selectivity. It may be caused by that too much Al dopant decreases the adsorption of oxygen.

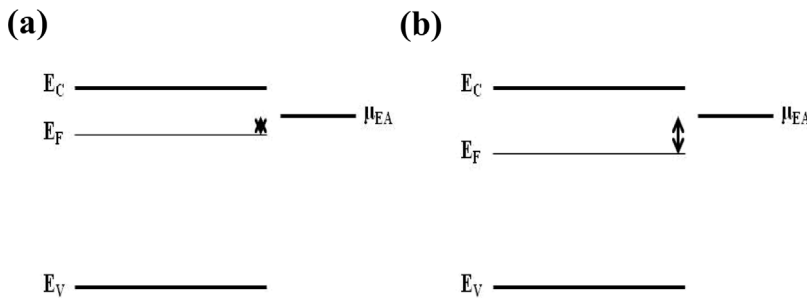


Fig. 14. Energy band diagram of (a) pure In_2O_3 , (b) Al-doped In_2O_3 . μ_{EA} represents the chemical potential of ethyl acetate molecule.

4. Conclusions

In summary, pure and Al-doped In_2O_3 were successfully synthesized and their ethyl acetate sensing properties were investigated. Compared with pure In_2O_3 gas sensor, it could be confirmed that 5 at% Al-doped In_2O_3 gas sensor exhibited enhanced ethyl acetate sensing properties, including higher response, lower detection limit and better selectivity. The excellent gas sensing performance of Al-doped In_2O_3 gas sensor might be attributed to the larger chemical potential gradient (the absorbed ethyl acetate and the Al-doped In_2O_3) caused more electrons transfer and grain size decreased. The results confirmed that Al-doped In_2O_3 gas sensor was a promising candidate for detecting ethyl acetate.

Acknowledgements

This work was supported by the National Natural Science Foundation of China (Grant No. 11574110), Project of Science and Technology Development Plan of Jilin Province (Grant No. 20160204013GX), Postdoctoral Science Foundation of China (Grant No. 2016M600231), Opened Fund of the State Key Laboratory on Applied Optics, Opened Fund of the State Key Laboratory on Integrated Optoelectronics, and State Grid Corporation of China (SGRIDGKJ[2015]959).

References

- [1] M. McCulloch, T. Jezierski, M. Broffman, A. Hubbard, K. Turner, T. Janecki, Diagnostic accuracy of canine scent detection in early- and late-stage lung and breast cancers, *Integr. Cancer Ther.* 5 (2006) 30–39.
- [2] H. Sonoda, S. Kohnoe, T. Yamazato, Y. Satoh, G. Morizono, K. Shikata, et al., Colorectal cancer screening with odour material by canine scent detection, *Gutgut*. 2010 218305 (2011).
- [3] Y. Duan, Current status of methods and techniques for breath analysis, *Crit. Rev. Anal. Chem.* 37 (2007) 3–13.
- [4] J. Ferlay, I. Soerjomataram, M. Ervik, R. Dikshit, S. Eser, C. Mathers, et al., GLOBOCAN 2012 v1.0, cancer incidence and mortality worldwide: IARC, CancerBase (2013) 2014.
- [5] N. Funazaki, A. Hemmi, S. Ito, Y. Asano, Y. Yano, N. Miura, et al., Application of semiconductor gas sensor to quality control of meat freshness in food industry, *Sens. Actuators B* 25 (1995) 797–800.
- [6] H.-J. Kim, K.-I. Choi, K.-M. Kim, C.W. Na, J.-H. Lee, Highly sensitive $\text{C}_2\text{H}_5\text{OH}$ sensors using Fe-doped NiO hollow spheres, *Sens. Actuators B* 171 (2012) 1029–1037.
- [7] K.M. Li, Y.J. Li, M.Y. Lu, C.I. Kuo, L.J. Chen, Direct conversion of single-layer SnO nanolayers to multi-layer SnO_2 nanoplates with enhanced ethanol sensing properties, *Adv. Funct. Mater.* 19 (2009) 2453–2456.
- [8] J. Huang, X. Xu, C. Gu, W. Wang, B. Geng, Y. Sun, et al., Effective VOCs gas sensor based on porous SnO_2 microcubes prepared via spontaneous phase segregation, *Sens. Actuators B* 173 (2012) 599–606.
- [9] T. Waitz, T. Wagner, T. Sauerwald, C.D. Kohl, M. Tiemann, Ordered mesoporous In_2O_3 : synthesis by structure replication and application as a methane gas sensor, *Adv. Funct. Mater.* 19 (2009) 653–661.
- [10] X. Sun, H. Hao, H. Ji, X. Li, S. Cai, C. Zheng, Nanocasting synthesis of In_2O_3 with appropriate mesostructured ordering and enhanced gas-sensing property, *ACS Appl. Mater. Interfaces* 6 (2013) 401–409.
- [11] S. Agarwala, Z. Lim, E. Nicholson, G. Ho, Probing the morphology-device relation of Fe_2O_3 nanostructures towards photovoltaic and sensing applications, *Nanoscale* 4 (2012) 194–205.
- [12] L. Wang, Z. Lou, T. Fei, T. Zhang, Zinc oxide core–shell hollow microspheres with multi-shelled architecture for gas sensor applications, *J. Mater. Chem.* 21 (2011) 19331–19336.
- [13] Z. Jing, J. Zhan, Fabrication and gas-sensing properties of porous ZnO nanoplates, *Adv. Mater.* 20 (2008) 4547–4551.
- [14] M.-H. Seo, M. Yuasa, T. Kida, J.-S. Huh, N. Yamazoe, K. Shimane, Microstructure control of TiO_2 nanotubular films for improved VOC sensing, *Sens. Actuators B* 154 (2011) 251–256.
- [15] T. Hyodo, H. Inoue, H. Motomura, K. Matsuo, T. Hashishin, J. Tamaki, et al., NO_2 sensing properties of macroporous In_2O_3 -based powders fabricated by utilizing ultrasonic spray pyrolysis employing polymethylmethacrylate microspheres as a template, *Sens. Actuators B* 151 (2010) 265–273.
- [16] Y. Wang, Y. Lin, D. Jiang, F. Li, C. Li, L. Zhu, et al., Special nanostructure control of ethanol sensing characteristics based on $\text{Au}/\text{In}_2\text{O}_3$ sensor with good selectivity and rapid response, *RSC Adv.* 5 (2015) 9884–9890.
- [17] J.T. McCue, J.Y. Ying, SnO_2 – In_2O_3 nanocomposites as semiconductor gas sensors for CO and NOx detection, *Chem. Mater.* 19 (2007) 1009–1015.
- [18] G. Korotcenkov, A. Cerneavscu, V. Brinzari, A. Vasilev, M. Ivanov, A. Cornet, et al., In_2O_3 films deposited by spray pyrolysis as a material for ozone gas sensors, *Sens. Actuators B* 99 (2004) 297–303.
- [19] Y. Shigesato, S. Takaki, T. Haranoh, Electrical and structural properties of low resistivity tin-doped indium oxide films, *J. Appl. Phys.* 71 (1992) 3356–3364.
- [20] A. Gurla, M. Ivanovskaya, N. Barsan, M. Schweizer-Berberich, U. Weimar, W. Göpel, et al., Grain size control in nanocrystalline In_2O_3 semiconductor gas sensors, *Sens. Actuators B* 44 (1997) 327–333.
- [21] M. Liess, Electric-field-induced migration of chemisorbed gas molecules on a sensitive film—a new chemical sensor, *Thin Solid Films* 410 (2002) 183–187.
- [22] C. Wang, X. Cheng, X. Zhou, P. Sun, X. Hu, K. Shimane, et al., Hierarchical α - Fe_2O_3 / NiO composites with a hollow structure for a gas sensor, *ACS Appl. Mater. Interfaces* 6 (2014) 12031–12037.
- [23] X. Cao, Y. Tao, L. Li, Y. Liu, Y. Peng, J. Li, An ethyl acetate sensor utilizing cataluminescence on Y_2O_3 nanoparticles, *Luminescence* 26 (2011) 5–9.
- [24] S.C. Navale, V. Ravi, D. Srinivas, I.S. Mulla, S.W. Gosavi, S.K. Kulkarni, EPR and DRS: evidence for NO_2 sensing in Al-doped ZnO , *Sens. Actuators B Chem.* 130 (2008) 668–673.
- [25] J. Gan, X. Lu, J. Wu, S. Xie, T. Zhai, M. Yu, et al., Oxygen vacancies promoting photoelectrochemical performance of In_2O_3 nanocubes, *Sci. Rep.* 3 (2012) 1021.
- [26] B. Li, Y. Xie, M. Jing, G. Rong, Y. Tang, G. Zhang, In_2O_3 hollow microspheres: synthesis from designed $\text{In}(\text{OH})_3$ precursors and applications in gas sensors and photocatalysis, *Langmuir* 22 (2006) 9380–9385.
- [27] D. Briggs, Handbook of X-ray Photoelectron Spectroscopy, in: C.D. Wanger, W.M. Riggs, L.E. Davis, J.F. Moulder, G.E. Muilenberg (Eds.), Perkin-Elmer Corp., Physical Electronics Division, Eden Prairie, Minnesota, USA, 1979, 190 pp., \$195, Surface & Interface Analysis, 3 (1981) v–v.
- [28] N.M. Figueiredo, N.J.M. Carvalho, A. Cavaleiro, An XPS study of Au alloyed Al–O sputtered coatings, *Appl. Surf. Sci.* 257 (2011) 5793–5798.
- [29] J.C. Dupin, D. Gonbeau, P. Vinatier, A. Levasseur, Systematic XPS studies of metal oxides, hydroxides and peroxides, *Phys. Chem. Chem. Phys.* 2 (2000) 1319–1324.
- [30] G. Carotenuto, G.P. Pepe, L. Nicolais, Preparation and characterization of nano-sized Ag/PVP composites for optical applications, *Eur. Phys. J. B* 16 (2000) 11–17.
- [31] A. Latore-Sanchez, J.A. Pomposo, A simple, fast and highly sensitive colorimetric detection of zein in aqueous ethanol via zein-pyridine-gold interactions, *Chem. Commun.* 51 (2015) 15736.
- [32] J. Qi, J. Chen, G. Li, S. Li, Y. Gao, Z. Tang, Facile synthesis of core–shell Au/CeO_2 nanocomposites with remarkably enhanced catalytic activity for CO oxidation, *Energy Environ. Sci.* 5 (2012) 8937–8941.
- [33] S.-q Guo, X. Zhang, Z.-w. Hao, G.-d. Gao, G. Li, L. Liu, In_2O_3 cubes: synthesis, characterization and photocatalytic properties, *RSC Adv.* 4 (2014) 31353–31361.
- [34] Qun Tang, Wenjia Zhou, W. Zhang, Shaomin Ou, K. Jiang, A. Weichao Yu, et al., Size-Controllable growth of single crystal $\text{In}(\text{OH})_3$ and In_2O_3 nanocubes, *Cryst. Growth Des.* 5 (2005) 147–150.
- [35] S. Wang, B. Xiao, T. Yang, P. Wang, C. Xiao, Z. Li, et al., Enhanced HCHO gas sensing properties by Ag-loaded sunflower-like In_2O_3 hierarchical nanostructures, *J. Mater. Chem. A* 2 (2014) 6598–6604.

- [36] P. Sun, Y. Sun, J. Ma, L. You, G. Lu, W. Fu, et al., Synthesis of novel SnO₂/ZnSnO₃ core–shell microspheres and their gas sensing properties, *Sens. Actuators, B* 155 (2011) 606–611.
- [37] G. Neri, A. Bonavita, G. Micali, G. Rizzo, E. Callone, G. Carturan, Resistive CO gas sensors based on In₂O₃ and InSnO_x nanopowders synthesized via starch-aided sol–gel process for automotive applications, *Sens. Actuators B* 132 (2008) 224–233.
- [38] N.J. Dayan, S. Sainkar, R. Karekar, R. Aiyer, Formulation and characterization of ZnO: Sb thick-film gas sensors, *Thin Solid Films* 325 (1998) 254–258.
- [39] B. Varghese, C. Teo, Y. Zhu, M.V. Reddy, B.V. Chowdari, A.T.S. Wee, et al., Co₃O₄ nanostructures with different morphologies and their field-emission properties, *Adv. Funct. Mater.* 17 (2007) 1932–1939.
- [40] J. Park, X. Shen, G. Wang, Solvothermal synthesis and gas-sensing performance of Co₃O₄ hollow nanospheres, *Sens. Actuators B* 136 (2009) 494–498.
- [41] N. Yamazoe, G. Sakai, K. Shimano, Oxide semiconductor gas sensors, *Catal. Surv. Asia* 7 (2003) 63–75.
- [42] X. Xu, H. Fan, Y. Liu, L. Wang, T. Zhang, Au-loaded In₂O₃ nanofibers-based ethanol micro gas sensor with low power consumption, *Sens. Actuators B* 160 (2011) 713–719.
- [43] M. Ivanovskaya, D. Kotsikau, G. Faglia, P. Nelli, Influence of chemical composition and structural factors of Fe₂O₃/In₂O₃ sensors on their selectivity and sensitivity to ethanol, *Sens. Actuators B* 96 (2003) 498–503.
- [44] G. Korotcenkov, I. Boris, V. Brinzari, S.H. Han, B.K. Cho, The role of doping effect on response of the SnO₂-based thin film gas sensors: analysis on the example of Co-doped SnO₂ films deposited by spray pyrolysis, *Sens. Actuators B Chem.* 182 (2013) 112–124.
- [45] Y. Wang, D. Jiang, W. Wei, L. Zhu, L. Shen, S. Wen, et al., Three dimensions sphere formaldehyde nanosensor applications: preparation and sensing properties, *RSC Adv.* 5 (2015) 50336–50343.
- [46] F. Li, Q. Qin, N. Zhang, C. Chen, L. Sun, X. Liu, et al., Improved gas sensing performance with Pd-doped WO₃H₂O nanomaterials for the detection of xylene, *Sens. Actuators B Chem.* 244 (2017) 837–848.

Biographies

Jingli Shen is an undergraduate in College of Electronic Science and Engineering, Jilin University, China, and interested in functional nanomaterials, chemical sensors.

Feng Li is an undergraduate in College of Electronic Science and Engineering, Jilin University, China and interested in nanomaterials and chemical sensors.

Bo Yin is an undergraduate in College of Electronic Science and Engineering, Jilin University, China, and interested in nanomaterials and chemical sensors.

Liang Sun is a senior engineer with the Master degree and mainly devotes to the research of material synthesis and electronic functional materials.

Chuan Chen is a senior engineer with the Master degree and mainly devotes to the research of gas sensing materials.

Shanpeng Wen received the PhD degree from Jilin University and mainly devotes to the research of gas sensing materials.

Yu Chen received the PhD degree from Institute of Semiconductors, Chinese Academy of Sciences in 2007. Now he is an associate researcher fellow and mainly devotes to the research of material synthesis and electronic functional materials.

Shengping Ruan received the PhD degree of electronic science and engineering from Jilin University in 2001. Now, he is a full professor in the College of Electronics Science and Engineering, Jilin University, and mainly devoted to the research of electronic functional materials and devices.